

collimated  $1 \mu\text{Ci } ^{241}\text{Am}$  alpha source to scans across the crystal surface.

## FARCOS composition

FARCOS is composed of telescopes forming clusters, where each cluster contains double-sided silicon-strip detectors (DSSSD) of 300 and 1500  $\mu\text{m}$  of thickness, as first and second stages, respectively, followed by 4 CsI(Tl) crystals arranged in 2x2 configuration of  $6 \times 32 \times 32 \text{mm}^3$ , as a third stage. Each DSSSD is divided into 32 horizontal and 32 vertical strips, with which it is possible to generate individual pixels of  $2 \times 2 \text{mm}^2$ . The total detection area of the silicon detectors is  $64 \times 64 \text{mm}^2$ , adapted to cover the total area of the 4 CsI(Tl) crystals placed behind. The scheme of the different stages of one FARCOS cluster is shown on Figure 1.

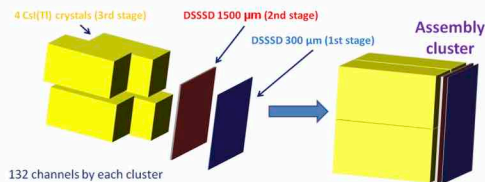


Figure 1: Different detection stages of the FARCOS array.

The current features of the different stages of the FARCOS array will allow achieving a high resolution not only when measuring energy but also in the determination of polar and azimuthal angles,  $\theta$  and  $\phi$ . The basic idea is the capability of building different geometries grouping the FARCOS clusters in various configurations.

As it was mentioned before, FARCOS is composed of CsI(Tl) crystals and DSSSD detectors. The first ones are highly doped CsI(Tl) crystals manufactured by SCIONIX [10]. Each crystal is wrapped with 0.12 mm thick white reflector including 50 micron of aluminized Mylar. The entrance window is composed by 2  $\mu\text{m}$  thick aluminized Mylar with a density of  $0.29 \text{ g/cm}^2$ . The Tl concentration is of the order of 1200 to 1500 ppm; higher concentrations are not recommended since it can produce a higher self-absorption. The output light is read by a Hamamatsu  $18 \times 18 \text{ mm}$  PIN diode S3204-08, attached to the rear face of each crystal.

In the case of DSSSD, they are manufactured by MICRON Semiconductor [11], based on a standard design (BB7) with a minimum area PCB frame (4 mm of length). Each detector has two kapton cables welded to two perpendicular sides of the detector, for BIAS and readout issues. Each cable manages the signal of 32 strips from junction and ohmic faces of each detector respectively. In addition, a common

ground and a BIAS guard-ring can also be managed with kapton cables.

## Experimental details on DSSSD

Concerning silicon strip detectors, they have been tested at the INFN Sezione di Catania. This test-lab can be used to test detectors with an acceptable vacuum level. A picture of a current silicon strip test setup is depicted on Figure 2.



Figure 2: FARCOS DSSSD mounted for test inside of a small chamber at Test-Lab at Sezione di Catania. In the down right corner, it can also be seen a motherboard to manage the signal and supply of two CsI(Tl) crystals.

To perform these tests, the electronic chain for 64 channels and a data acquisition station were mounted. It included commercial preamplifiers Mesytec, amplifiers CAEN N1568B 16Ch PSA PSD and 32-channel QDC CAEN modules. 32 additional digital channels were also included, in order to use CsI(Tl) crystal during the test along with silicon. In this campaign, 8 DSSSD detectors (4 of 300  $\mu\text{m}$  and 4 of 1500  $\mu\text{m}$ ) were tested with a triple-alpha source, observing a very well resolution in all of them. In many occasions the signal of one or two CsI(Tl) crystals was included on the trigger to test the behaviour of both different types of detectors simultaneously. Figure 3. shows a typical alpha source spectrum where a high energy resolution of 30 keV is attained.

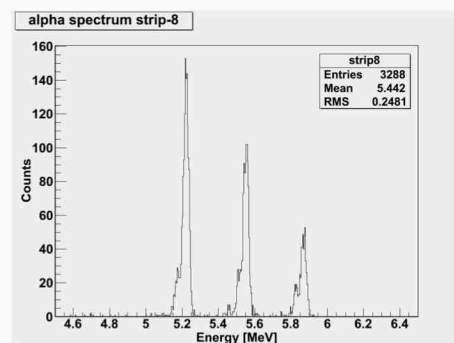


Figure 3: Typical calibrated spectrum obtained

during the test of FARCOS silicon detectors. A high energy resolution can be observed on the triple alpha peaks.

## Experimental details on CsI crystals

In order to test the position dependence of the response of the CsI crystals to 5.486 MeV alpha particles from a  $^{241}\text{Am}$  source, a test apparatus was built, which allows one to move a collimated alpha source respect to CsI(Tl) crystal in perpendicular directions inside a vacuum chamber.



Figure 4: Meccanical scanning for the FARCOS CsI crystals inside the chamber with a collimated  $^{241}\text{Am}$  source.

The configuration was automated such that an energy spectrum was obtained for points separated by a spacing of 2.7 mm on a 3 by 3 Cartesian grid on the front surface of the test crystals. This grid was centered on the crystals. At each grid point, the collimated source irradiated a circular area of the crystal surface for 15 minutes before moving to the next grid point. The meccanical scanning source test configuration is shown on Figure 4.

Our priority is now to determine the relative position of the edges of the detector along the x and y axes with respect to the lower limit of the motorized slides (this will represent the absolute zero

position) which are known by a sensor. Each CsI (Tl) crystal subsequently tested will always have the same relative coordinates with respect to this absolute zero point thanks to a mask that contains it (see Figure 4).

The edges of the detector can be determined by the fit of the spectrum of the counts of the alpha particles, recorded in a fixed time interval (in our case 15 minutes), depending on the position both along the x and y axes. Infact, the number of alpha particles that hit the detector are equal to the mean value of the counts recorded when the beam spot is completely inside of the detector weighed to the fraction of the circular sector intercepted by the crystal, as shown in Figure 5.

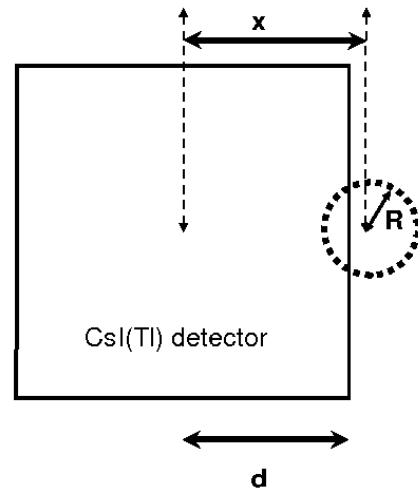


Figure 5: Circular sector intercepted on the CsI(Tl) crystal.

It is then possible to fit the distribution of counts of the alpha particles as a function of position by means of the following formula:

$$N(d) = N_0 \left[ 1 - \frac{1}{\pi} \arccos\left(\frac{x-d}{R}\right) - \sqrt{1 - \left(\frac{x-d}{R}\right)^2} \left(\frac{x-d}{R}\right) \right] \quad (1)$$

when  $-1 < \frac{x-d}{R} < 1$ ,  $N(d) = N_0$  when  $\frac{x-d}{R} < -1$  and  $N(d) = 0$  when  $\frac{x-d}{R} > 1$ , where d is the edge coordinate of the detector,  $N_0$  the number of hits when the alpha beam spot is entirely on detector and R the radius of the beam spot (all free parameters of the fit).

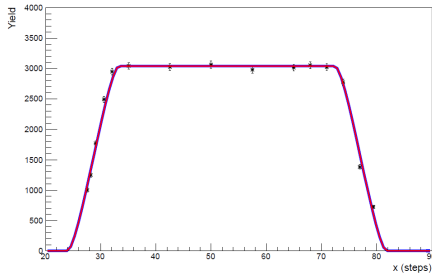


Figure 6: fit of the distributions of the experimental points along the x axis.

Figure 6 shows the fit of the distributions of the experimental points along the x direction. The same fit was conducted in y direction.

Using the information from the linear drives used to move the source, discrete grids in the x-y coordinate plane are mapped onto the scintillation crystals. At the coordinate  $x = i$ ,  $y = j$ , the non-uniformity  $S_{ij}$  of light output for scintillation crystals is expressed as:

$$S_{ij} = \frac{L_{ij} - \langle L \rangle}{\langle L \rangle} \quad (2)$$

where  $L_{ij}$  is the centroid of the energy spectrum at position  $(i, j)$  and  $\langle L \rangle$  is the average over the entire crystal. In the case of a crystal with a perfectly uniform response, the variance of  $S_{ij}$  would be dictated only by the statistical uncertainty of the centroids of the peaks. In practice, the variance of  $S_{ij}$  can be dominated by the light output non-uniformity in each crystal. The centroid of the light output peak was calculated for each of the Cartesian grid points. Figure 7 shows the  $S_{ij}$  calculated from Equation 2 for one test crystal. This crystal shows a very good uniformity (better than 1%). In the Figure 8 we show a crystal where a non-uniformity larger than 5% is observed when moving from one edge to the other. Furthermore, a gradient in the light response is observed as a function of the x-y position on the surface. In the case of non-uniform crystals like the one shown on Figure 7, it will be important to study the position dependence of light response with higher energy alpha particles injected directly by the CS of the LNS. These tests are going to be carried out in summer 2012 with the aim of obtaining position-dependent correction factor in light spectra measurements performed by CsI(Tl).

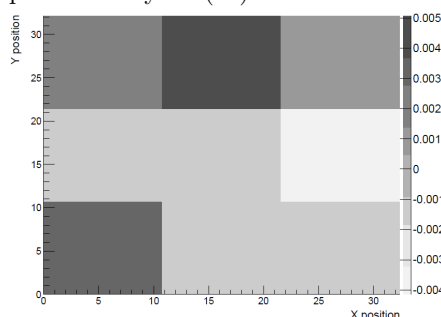


Figure 7: Light response spectra in grey scale for the FARCOS CsI crystal serial number SBG055.

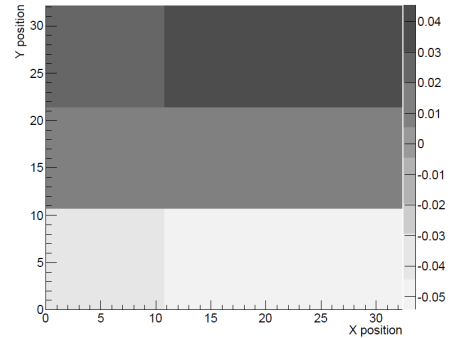


Figure 8: Light response spectra in grey scale for the FARCOS CsI crystal serial number SBG052.

## Conclusions and perspectives

From the analysis conducted in this work we have evaluated both the resolution of DSSSD and the surface variation of light response in CsI(Tl) crystals. The test with alpha source explore only the surface of the crystal. Further studies must be performed to evaluate the variation in depth of the detector with different beams at high energy delivered by the CS of the LNS. These tests with beams was performed in summer 2012 and the results are being analyzed.

## References

- [1] G. Verde et al., Eur. Phys. J. A **30**, 81 (2006).
- [2] J. Pouthas et al., Nucl. Instr. and Meth. A **357**, 418 (1995).
- [3] A. Pagano et al., Nucl. Phys. A **681**, 331c (2001).
- [4] G. Verde et al., Phys. Rev. C **65**, 054609 (2002).
- [5] G. Verde et al., Phys. Rev. C **67**, 034606 (2003).
- [6] P.Schotanus and R.Kamermans. IEEE Trans. Nucl. Sci., **37**, 177 (1990).
- [7] A. Wagner et al., Nucl. Instr. and Meth. A, **456**, 290 (2001).
- [8] A. Wagner et al., Nucl. Instr. and Meth. A, **456**, 290 (2001).
- [9] J.B.Birks. Theory and Practice of Scintillation Counters. Pergammon Press, Oxford, (1964).
- [10] ] <http://www.scionix.nl/>.
- [11] <http://www.micronsemiconductor.co.uk/>.

## Meson Photoproduction and Baryon Resonances at MAMBO experiment

M. Romaniuk<sup>1,2</sup>, F. Curciarello<sup>1,2</sup>, V. De Leo<sup>1,2</sup>, G. Mandaglio<sup>1,2</sup>, G. Giardina<sup>1,2</sup>

<sup>1</sup>*Dipartimento di Fisica e di Scienze della Terra, Universita di Messina, I-98166, Messina, Italy*

<sup>2</sup>*INFN- Sezione Catania, I-95123, Catania, Italy*

E-mail: mromaniuk@unime.it

### Abstract

Photoproduction of mesons within the framework of the MAMBO experiment (BGO-OD at Bonn plus MAMI at Mainz) was studied. The results on the operative work of the cryogenic  $H_2/D_2$  target system during the last commissioning beam times at the March and June 2012 are shown. Investigation of the single charged pion photoproduction was provided using a polarized  $^3\text{He}$  target at the tagged photon facility of the MAMI accelerator. Unpolarized and helicity dependent cross sections are presented for channels  $\gamma N \rightarrow \pi^\pm X$  in the  $\Delta(1232)$  baryon resonance region.

**Keywords:** pion photoproduction, cryogenic  $H_2/D_2$  target system, helicity dependent cross section.

## BGO–OD collaboration

Nowadays the question of the hadron structure still exist in understanding of some specific states at range of quark models. To investigate baryon resonances we use the photoproduction of mesons. Electromagnetic probe is a good tool for the study of nucleon resonances since it is possible to get access to resonance states coupled to photons and also polarization observables are accessible, which give us separation of overlapping resonances. In order to obtain full information about baryonic resonances it is need to study different channels: non-strange pseudoscalar mesons with charge combinations, strange and vector mesons.

The new experimental setup of the recently established BGO–OD collaboration consists of the combination of an open-dipole forward spectrometer and the BGO ball which cover the central angular region. This configuration is ideally suited to investigate the photoproduction of multi-particle final states with mixed charges. In addition it will allow nucleon polarization measurements in single-meson photoproduction. Due to the excellent forward acceptance it opens the possibility to investigate vector-meson production in order to understand the reaction mechanism and the role of resonances. The BGO–OD collaboration presently includes individuals and groups from Germany (Bonn), Italy (Rome, Frascati, Pavia, Messina), Russia (Gatchina, Moscow), UK (Edinburgh, Glasgow) and Ukraine (Kharkov).

The experimental set-up (see Fig. 1) consists of a large 90 ton dipole magnet, tracing detectors, two

scintillating fiber detectors, MOMO and SciFi2 (to allow for momentum reconstruction of charged particles bent through the magnetic field), an aerogel Cherenkov detector (discriminates pions against protons and particularly improves the K-identification substantially), a time-of-flight (TOF) detector (provides flight-time measurements for charged particles and neutrons), the BGO Ball which is optimized for photon detection, good performances with protons (energy and angle reconstruction) and good neutron detection efficiency. BGO hermetically encloses the target (polar angular range 25–155 degrees). Main features of BGO–OD beam: Beam energy :  $E_\gamma = 0.7 - 2.8$  GeV; linear polarization degree up to 2.0 – 2.2 GeV; high intensity ( $10^7 \gamma/s$ ) for low cross section reactions [1]. The Quantumcooler Hydrogen/Deuterium is a two stage closed-cycle refrigerator. The working fluid in all stages is an high purity helium gas. The nominal operating temperatures of each stage is 70 K and 20 K, respectively. Both stages are based on the Gifford-McMahon (G–M) cycle. The target cell is a 3 cm diameter aluminum cylinder, closed by thin mylar windows at the two sides. Two different lengths of the cell 6 cm and 11 cm are available.

The target cell could be filled with liquid Hydrogen ( $H_2$ ) or Deuterium ( $D_2$ ). The hydrogen/deuterium gas is cooling down by the helium through heat exchangers and liquefied inside the cell. In order to ensure the movement of the target system and and extraction of the nose out of the BGO the rails system was build, see Fig. 2.

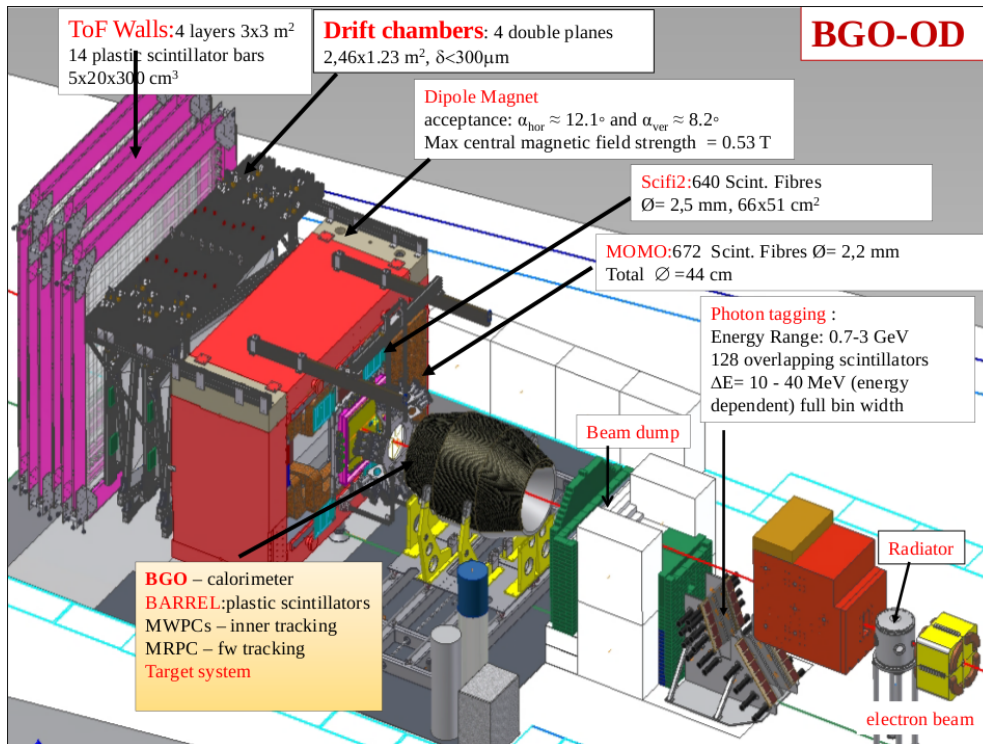


Figure 1: Overview of the experimental set up of the BGO–OD experiment

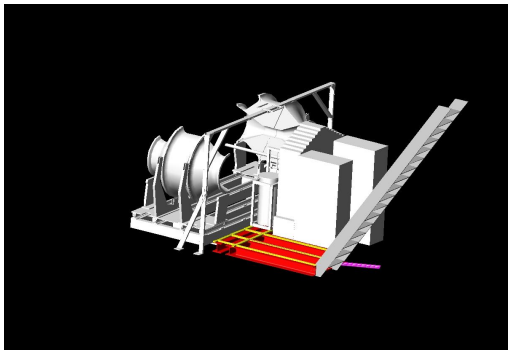


Figure 2: Schematic view of the target system, BGO ball and rails system

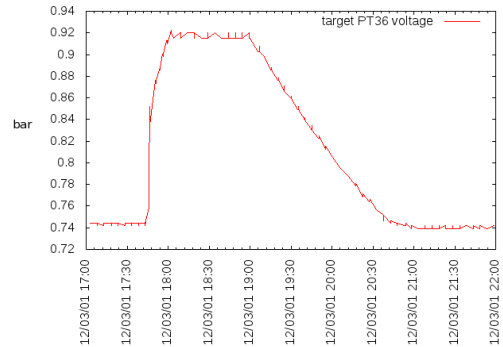


Figure 3: Pressure on target cell during emptying and fill back; pressure +0.74 bar – cell is full, pressure +0.92 bar – target cell is empty [2]

Initial cool-down of the  $H_2$  from room temperature take about 8 hours; it is possible to empty cell in  $\sim 20$  minutes using electric heater, refill target in  $\sim 2$  hour.

On the Figure 3 presented pressure on the target cell during commissioning beam time at March 2012. Pressure 0.74 bar corresponds to the cell full with liquid hydrogen, 0.92 bar corresponds to the empty cell.

During beam time in June 2012 a new behavior of the pressure was detected.

There was some fluctuation of the supply and return pressures with time, which could be explained by day/night change of the temperature in the experimental area, see Fig. 4, 5.

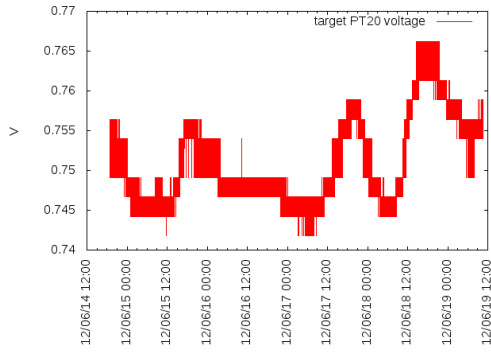


Figure 4: Fluctuation of the full cell pressure during beam time in June, 2012

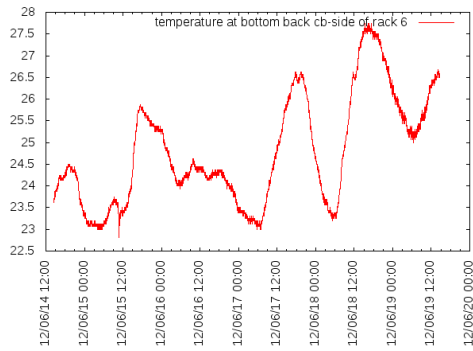


Figure 5: Fluctuation of the temperature of the experimental area during beam time in June, 2012

During this year target system was installed at the experimental area, all safety procedure was completed, one check run was performed and two runs during beam times (one two weeks long, second one week long) were performed. Target system works in a proper way, line for  $H_2$  is stable.

## A2 collaboration

Another important subject in study of the baryon resonances is helicity dependent variables (especially on neutron), which provide better understanding of the reaction mechanism and structure effects.  ${}^3\text{He}$  is a system consisting of two protons with spins paired off and an active unpaired neutron, in relative s state with 90% probability. As a result, magnetic moment of  ${}^3\text{He}$  can be approximated with the magnetic moment of the neutron:  $\mu^{{}^3\text{He}} \approx \mu_n$ .

During July, 2009 a first measurement of the double polarized photoabsorption cross section on  ${}^3\text{He}$  in the  $\Delta(1232)$  baryon resonance region has been performed at the tagged photon facility of the MAMI accelerator in Mainz. Circularly polarized photons were obtained by bremsstrahlung of longitudinally polarized electrons with an average polarization of 75%, the bremsstrahlung photons were tagged using the

Glasgow-Mainz magnetic spectrometer (energy resolution  $\sim 2$  MeV). The relative tagging efficiency was monitored by a CCD photon camera and absolute measurements were made using a lead-glass detector. The reaction products were detected by the central detector system (see Fig. 6) consisting of the Crystal Ball (CB) NaI spectrometer, complemented by the Multi-Wire Proportional Chambers (MWPCs), used to identify and track the charged particles, and the cylindrical Particle Identification Detector (PID), used to distinguish the charged from the neutral particles detected by the CB. The combined information provided by these three detectors provides accurate energy, angle and particle identification in the azimuthal ( $\varphi$ ) and polar ( $\theta$ ) angular regions from  $0^\circ$  to  $360^\circ$  and from  $21^\circ$  to  $159^\circ$ , respectively.

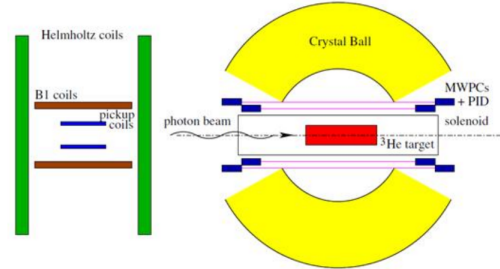


Figure 6: Side view of the central detectors setup

## Results and conclusions

Using  $dE/dx$  vs  $E$  technique, PID and MWPCs information pion/proton separation has been done. Preliminary results obtained for unpolarised total cross section as a function of the incoming photon energy up to 500 MeV for  $\gamma^3\text{He} \rightarrow \pi^\pm N$  channels are shown in Fig. 7, where data (blue spots) are compared to the predictions from the model of A.Fix (red line) [3].

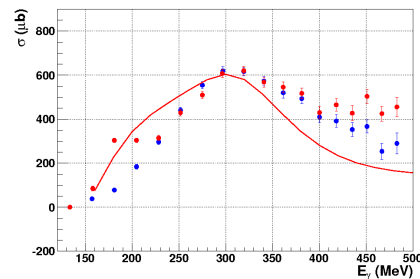


Figure 7: Unpolarised total cross section as a function of the incoming photon energy up to 500 MeV for  $\gamma^3\text{He} \rightarrow \pi^\pm N$  channels

Fix's model take into account Fermi motion of the interacting nucleons inside the nuclei and the nuclear effects, final state interaction (FSI)

taken into account in an approximate way. Unpolarized differential cross section compared to the predictions from the Fix's model (red line) and to the MAID model (dashed black line), which consider the protons and the neutron inside  ${}^3\text{He}$  behave as free nucleons, see Fig. 8.

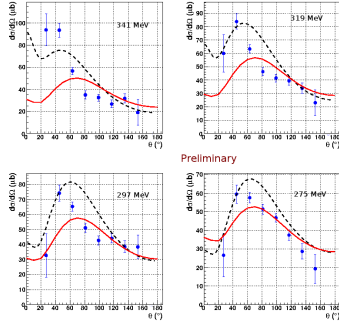


Figure 8: Unpolarised differential cross section as a function of the incoming photon energy up to 500 MeV for  $\gamma^3\text{He} \rightarrow \pi^\pm N$  channels

In the Fig. 9 the total helicity dependent cross section difference,  $\Delta\sigma_\pi = \sigma_{\pi,a} - \sigma_{\pi,p}$ , for the  $\gamma^3\text{He} \rightarrow \pi^\pm N$  channels is shown in comparison to the predictions from Fix's model. In Fig. 10 shows preliminary results on the polarized differential cross section compared with the DAPHNE data [4] (obtained by deuteron target), the MAID and Fix model calculations. FSI plays important role at the low energy region, for both unpolarized and polarized cases, but in high energy region there is disagreement between the data and Fix's model prediction.

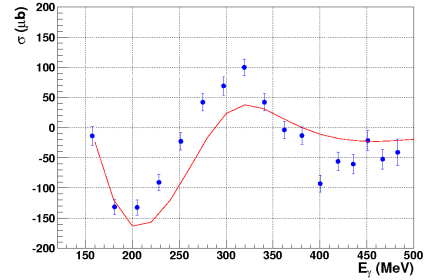


Figure 9: Polarised total cross section as a function of the incoming photon energy up to 500 MeV for  $\gamma^3\text{He} \rightarrow \pi^\pm N$  channels

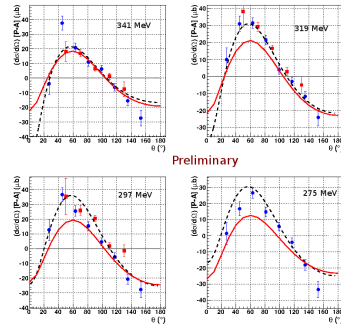


Figure 10: Polarised differential cross section as a function of the incoming photon energy up to 500 MeV for  $\gamma^3\text{He} \rightarrow \pi^\pm N$  channels

## References

- [1] ELSA: *Letter to intent to the PAC*, 2009.
- [2] Romaniuk, M.: *Target system* Internal Note BGO-OD Collaboration, 2012.
- [3] Fix, A.: *Private communication*, 2012.
- [4] Pedroni, P.: *Double polarization experiments at MAMI 12*. Eur. Phys. J. Topics, **198**, 2011, p. 12. 181–198.

## Analysis of CHIMERA data from ASY-EOS experiment

S. Santoro<sup>1,2</sup>, L. Acosta<sup>3</sup>, F. Amorini<sup>3</sup>, L. Auditore<sup>1,2</sup>, C. Boiano<sup>5</sup>, G. Cardella<sup>6</sup>, S. Cavallaro<sup>6,4</sup>, M. Colonna<sup>3</sup>, E. De Filippo<sup>6</sup>, M. Di Toro<sup>3,4</sup>, E. Geraci<sup>6,4</sup>, L. Grassi<sup>13</sup>, V. Greco<sup>3,4</sup>, C. Guazzoni<sup>5,7</sup>, P. Guazzoni<sup>5,8</sup>, R. Introzzi<sup>9</sup>, E. La Guidara<sup>6</sup>, G. Lanzalone<sup>3,10</sup>, I. Lombardo<sup>11,12</sup>, D. Loria<sup>1,2</sup>, T. Minniti<sup>1,2</sup>, A. Pagano<sup>6</sup>, M. Papa<sup>6</sup>, S. Pirrone<sup>6</sup>, G. Politi<sup>6</sup>, F. Porto<sup>3,4</sup>, F. Riccio<sup>5,8</sup>, F. Rizzo<sup>3,4</sup>, E. Rosato<sup>11,12</sup>, P. Russotto<sup>3,4</sup>, A. Trifiró<sup>1,2</sup>, M. Trimarchi<sup>1,2</sup>, G. Verde<sup>6</sup>, M. Vigilante<sup>11,12</sup>, P. Zambon<sup>5,7</sup>, L. Zetta<sup>5,8</sup> and ASY-EOS collaboration: M. Adamczyk<sup>14</sup>, A. Al-Ajlan<sup>15</sup>, M. Al-Garawi<sup>16</sup>, S. Al-Homaidhi<sup>15</sup>, T. Aumann<sup>17</sup>, Y. Ayyad<sup>18</sup>, V. Baran<sup>14,29</sup>, Z. Basrak<sup>13</sup>, J. Benlliure<sup>18</sup>, M. Boisjoli<sup>19</sup>, K. Boretzky<sup>20</sup>, J. Brzychczyk<sup>14</sup>, A. Budzanowski<sup>21</sup>, P. Cammarata<sup>22</sup>, Z. Chajecski<sup>23</sup>, M. Chartier<sup>24</sup>, A. Chbihi<sup>19</sup>, B. Czech<sup>21</sup>, M. Famiano<sup>25</sup>, A. Le Fevre<sup>20</sup>, I. Gašparić<sup>13</sup>, M. Heil<sup>20</sup>, L. Heilborn<sup>22</sup>, T. Isobe<sup>26</sup>, K. Kezzar<sup>16</sup>, M. Kiš<sup>20,13</sup>, S. Kupny<sup>14</sup>, N. Kurz<sup>20</sup>, P. Lasko<sup>14</sup>, Y. Leifels<sup>20</sup>, R. Lemmon<sup>27</sup>, Q. Li<sup>28</sup>, J. Lukasik<sup>21</sup>, W.G. Lynch<sup>23</sup>, P. Marini<sup>22</sup>, Z. Matthews<sup>24</sup>, L. May<sup>22</sup>, M. Mostazo<sup>18</sup>, P. Pawlowski<sup>21</sup>, M. Petrovici<sup>29</sup>, R. Reifarth<sup>20</sup>, W. Reisdorf<sup>20</sup>, H. Simon<sup>20</sup>, I. Skwirczynska<sup>21</sup>, Z. Sosin<sup>14</sup>, W. Trautmann<sup>20</sup>, B. Tsang<sup>23</sup>, M. Veselsky<sup>30</sup>, A. Wieloch<sup>14</sup>, P. Wigg<sup>24</sup>, H.H. Wolter<sup>31</sup>, P. Wu<sup>24</sup>, S. Yennello<sup>22</sup>, M. Zoric<sup>13</sup>

<sup>1</sup> INFN, Gr. Coll. di Messina, Italy

<sup>2</sup> University of Messina, Department of Physics and Earth Science, Italy

<sup>3</sup> INFN-LNS, Catania, Italy

<sup>4</sup> University of Catania, Department of Physics Italy

<sup>5</sup> INFN, Sezione di Milano, Italy

<sup>6</sup> INFN, Sezione di Catania, Italy

<sup>7</sup> Politecnico di Milano, Italy

<sup>8</sup> University of Milano, Department of Physics, Italy

<sup>9</sup> INFN, Politecnico di Torino, Italy

<sup>10</sup> Kore University of Enna, Italy

<sup>11</sup> INFN, Sezione di Napoli, Italy

<sup>12</sup> University of Napoli, Department of Physics, Italy

<sup>13</sup> RBI, Zagreb, Croatia

<sup>14</sup> Jagiellonian University, Kraków, Poland

<sup>15</sup> KACST, Riyadh, Saudi Arabia

<sup>16</sup> King Saud University, Riyadh, Saudi Arabia

<sup>17</sup> Technische Universität, Darmstadt, Germany

<sup>18</sup> University of Santiago de Compostela, Spain

<sup>19</sup> GANIL, Caen, France

<sup>20</sup> GSI, Darmstadt, Germany

<sup>21</sup> IFJ-PAN, Kraków, Poland

<sup>22</sup> Texas A&M University, College Station, TX, USA

<sup>23</sup> NSCL Michigan State University, MI, USA

<sup>24</sup> University of Liverpool, UK

<sup>25</sup> Western Michigan University, MI, USA

<sup>26</sup> RIKEN, Wako, Japan

<sup>27</sup> STFC Daresbury Laboratory, UK

<sup>28</sup> Huzhou Teachers College, China

<sup>29</sup> NIPNE, Bucharest, Romania

<sup>30</sup> Institute of Physics, Slovak Academy of Sciences Bratislava, Slovakia

<sup>31</sup> LMU, München, Germany

E-mail: ssantoro@unime.it

### Abstract

The elliptic-flow ratio of neutrons with respect to protons in reactions of neutron rich Heavy-Ion at intermediate energies has been proposed as an observable sensitive to the strength of the symmetry term in the nuclear Equation Of State (EOS) at supra-saturation densities. The recent results obtained from the existing FOPI/LAND data for  $^{197}\text{Au}+^{197}\text{Au}$  collisions at 400 MeV/nucleon in comparison with the UrQMD

model allowed a first estimate of the symmetry term of the EOS but suffer from a considerable statistical uncertainty. In order to obtain an improved data set for Au+Au collisions and to extend the study to other systems, a new experiment was carried out at the GSI laboratory by the ASY-EOS collaboration in May 2011.

## Introduction

In May 2011 the data taking of experiment S394 at GSI has been completed. The symmetric collision systems  $^{197}\text{Au} + ^{197}\text{Au}$ ,  $^{96}\text{Zr} + ^{96}\text{Zr}$  and  $^{96}\text{Ru} + ^{96}\text{Ru}$  at 400 MeV/nucleon incident energies have been measured. The main aim of the experiment is to measure the ratio of parameters describing the elliptic flow of neutrons and hydrogen isotopes in Heavy-Ion collisions at relativistic energies in order to obtain constraints on the behavior of the symmetry term of the nuclear equation of state (EOS) at supra-saturation densities [1]. Recently, an estimate of the high density behavior of the symmetry energy has been obtained from the re-analysis of the existing FOPI/LAND data for  $^{197}\text{Au} + ^{197}\text{Au}$  collisions at 400 MeV/nucleon. Comparison with predictions of the UrQMD transport model [2] favors a density dependence of the potential symmetry term proportional to  $(\rho/\rho_0)^\gamma$  with  $\gamma = 0.9 \pm 0.4$  [3]. The sensitivity of the proton-neutron elliptic flow difference to the symmetry energy has been more recently confirmed by calculations with the Tubingen version of the QMD transport model [4]. Moreover new data would be important to study isospin effects on the momentum dependence of the in-medium interactions [5]. With the new experiment (S394), an attempt is being made to considerably improve the previous set of data, by improving the statistical accuracy of the measured flow parameters for Au+Au reactions and to extend the flow measurements to other systems. Indeed the study of isospin effects can be improved using new observable like the one related to light fragments up to atomic number of about  $Z=4$ , with special emphasis on the light isobar pairs  $^3\text{H}/^3\text{He}$  and  $^7\text{Li}/^7\text{Be}$ .

## Experimental set-up

The Large Area Neutron Detector (LAND) [6], recently upgraded with new TACQUILA GSI-ASIC electronics, was positioned at laboratory angles around  $45^\circ$  with respect to the beam direction, at a distance of about 5 m from the target. A veto-wall of plastic scintillators in front of LAND allows discrimination of neutrons and charged particles. In such a way it is possible to measure the direct and elliptic collective flows of neutrons and hydrogen's at mid-rapidity with high precision in the same angular acceptance. In addition, Krakow Triple Telescope Array, KraTTA [7], covering polar angles between  $20^\circ$  and  $64^\circ$  at a distance of 40 cm from the target, permitted the acquisition of data upon yield and collective flows of light charged particles, up to  $Z \sim 5$ , at mid-rapidity. The determination of impact parameter and the orientation of the reaction plane required the use of several devices: i) the ALADIN Time-of-Flight plastic wall [8] was used to detect forward emitted charged particles at polar angles smaller than  $7^\circ$ ; two walls (front and rear) of  $2.5 \times 100 \text{ cm}^2$  plastic scintillators, read by two photo-multipliers at both edges, gave information on

emission angle, atomic number and velocity of ions; a Time Of Flight vs  $\Delta E$  scatter plots is shown in panel *d*) of Fig. 3, for a single scintillator; the different elements can be easily separated. The obtained time of flight resolution, with respect to the start detector, is  $\Delta t \sim 250 \text{ ps}$ , while  $\Delta Z/Z$  is  $\sim 5 \%$ . ii) 50 thin ( $\sim 1 \text{ cm}$  thick) CsI(Tl) elements, read by photo-diodes, arranged in 4 rings of the Washington-University  $\mu$ -ball array [9], covering polar angles between  $60^\circ$  and  $147^\circ$ , surrounded the target with the aim of measuring the distribution of backward emitted particles and to discriminate against background reactions on non-target material; iii) 352 CsI(Tl), 12 cm thick, scintillators of the CHIMERA multidetector [10], arranged in 8 rings in  $2\pi$  azimuthal coverage around the beam axis, covered polar angles between  $7^\circ$  and  $20^\circ$ , measuring the light charged particles. In addition thin ( $300 \mu\text{m}$ ) Silicon detector were placed in front of 32 (4 by ring) CsI detectors in the usual  $\Delta E$ -E configuration.

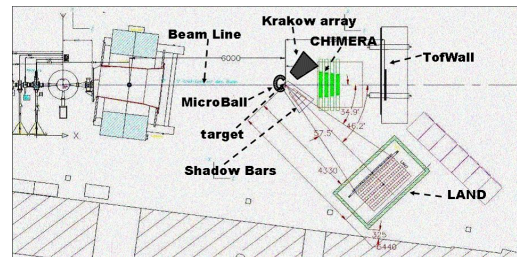


Figure 1: Schematic view of experimental setup

The beam was guided in vacuum to about 2 m upstream from the target. A thin plastic foil read by two Photo-multipliers was used to tag in time the beam arrival and acted as a start detector for time of flight measurement. A schematic view of the experimental set-up is given in Fig. 1.

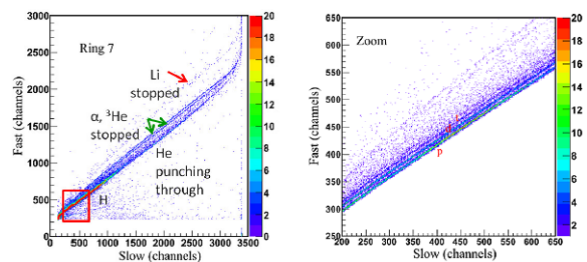


Figure 2: left panel: Fast vs Slow component scatter plot as obtained with a CHIMERA CsI(Tl) scintillator placed at a polar angle  $\theta_{lab} \sim 17^\circ$  for Au+Au reactions at 400 MeV/nucleon; lines of particles stopped CsI detector are indicated by arrows; the region highlighted by the square is zoomed on the right panel, showing (from bottom) lines of H punching through,  $^1\text{H}$  stopped,  $^2\text{H}$  stopped and  $^3\text{H}$  stopped

With beam intensities of about  $10^5$  pps and targets of

1-2% interaction probability, about  $5 \cdot 10^6$  events for each system were collected. Special runs were performed with and without target, in order to measure the background from interaction of projectile ions with air, and with iron shadow bars covering the angular acceptance of LAND in order to measure neutron background. Data acquisition was performed using the MBS data acquisition system available at GSI [11]; the CHIMERA data acquisition was integrated into the MBS system using the time-stamping technique for data synchronization. The analysis of the collected data has been started with calibrations of the individual detector systems and with overall quality checks, and is currently in progress. At the present stage we will report here only on some preliminary results from CHIMERA data.

## CHIMERA Preliminary results and outlook

Identification of Light Charged Particles in CHIMERA CsI(Tl) has been performed using Pulse Shape Analysis based on standard fast-slow techniques; an example is shown in Fig. 2. We have obtained isotopic identification for p,d,t and  $^3\text{He}$  ions stopped in the CsI detectors. Particles punching through the CsI(Tl) can be separated and identified (only in atomic number) by particles stopped in the scintillators; in fact the difference in ionization densities  $dE/dx$  between stopped and punching through ions results in a different fast/slow ratio. At the lowest fast and slow values, an intense ridge due to gamma, fast electrons, and background reactions on non-target material is found. For particles heavier than helium, the slow component is partially saturated, since the gate width for the CsI slow component has been chosen in order to compromise between a good separation of hydrogen isotopes and identification of Li/Be ions within the codifiers maximum energy range.

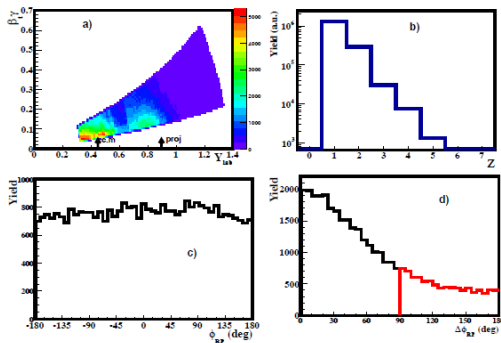


Figure 3: CHIMERA data for Au+Au system; a) transverse velocity versus rapidity in lab reference system; b) charge distribution; c) orientation of reaction plane obtained using Q-vector method; d) difference of orientations of reaction plane as obtained using sub-events mixing technique

The identification in CsI has been cross-checked with the one obtained in the 32 Si-CsI telescopes via  $\Delta E$ -E

technique. In addition, a digital acquisition sampling technique (14 bit, 50 MHz sampling) was used, in parallel to the standard analog one, in about 10 % of the detectors. Cross checking of identification between standard analog and digital technique has been of fundamental importance; more results are given in [12]. Energy calibration of the fast component has been performed via the evaluation of the punching through points. For particles punching through the detectors, the total kinetic energy has been evaluated from the measured  $\Delta E$  using energy loss tables. As a global result we show in panel a) of Fig. 3 the transverse velocity versus rapidity in the lab reference system for the Au + Au system. In order to reject fast electrons and background, a threshold of  $E/A > 50$  MeV/nucleon has been imposed. In the figure we can clearly see population of two intense regions around *mid-rapidity* and projectile rapidity; panel b) shows the obtained charge distribution. An important parameter is the resolution achieved in determining the azimuthal orientation of the reaction plane. It largely determines the uncertainty associated with the determined flow parameters [13]. As a first test we have estimated the reaction plane orientation for events with total charged particle multiplicity  $M \geq 10$  in CHIMERA, using the *Q*-vector method of Ref. [14].

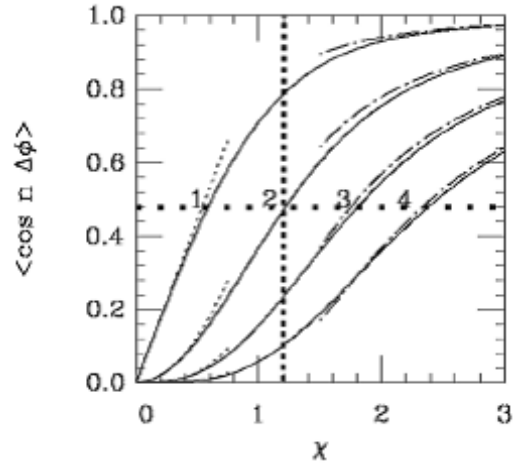


Figure 4: Correction curves for the first four harmonics  $v_n$  ( $n = 1 - 4$ ) of the azimuthal distribution as a function of the resolution parameter  $\chi$ . The obtained  $\chi \sim 1.2$  (dashed vertical line) implies a correction factor  $\langle \cos(2\Delta\phi) \rangle \sim 0.48$  for the elliptic flow parameter  $v_2$  (dotted horizontal line); picture adapted from [15]

In order to reject the mid-rapidity region, a cut on laboratory rapidity  $y > 0.548$  (corresponding to  $y > 0.1$  in c.m. system) was used. The obtained reaction plane distribution for a CHIMERA data sample from the  $^{197}\text{Au} + ^{197}\text{Au}$  data set is shown in panel c) of Fig. 3; the flatness indicates that the particle angular distributions have not been biased by the event triggering in the experiment. We also tested the resolution achieved in reconstructing the reaction plane using the sub-event mixing technique of Ref. [15]. The distribution of the difference between the two reaction plane orientations extracted by the sub-

events is reported in panel *d*) of Fig. 3. Using the method of [15] we obtain a reaction plane dispersion parameter  $\chi \sim 1.2$ , resulting in an attenuation of the elliptic flow measurement of  $\sim 0.5$ , as illustrated in Fig. 4, showing correction factors for the Fourier parameters of the azimuthal distribution  $v_n$  of order  $n$  as a function of  $\chi$ . The analysis performed so far shows that the particle identification achieved with the CHIMERA detector modules is better than the one estimated in experimental setup simulations. It is to be expected that these values will improve considerably as soon as the information collected with the Time-of-Flight wall and -ball can be included in the analysis.

## Data Simulation from CHIMERA

The UrQMD transport model has been used to simulate the proton-neutron elliptic flow for semi-central collision and to understand better its sensitivity to the symmetry energy [3].

In order to investigate the detector response, we have instead used UrQMD simulation as input in Geant3 package (included in the FairRoot framework), tracking the particles inside the CHIMERA CsI scintillators. The energy deposited in the scintillators has been transformed into light output using a Birk relation; an example of fast-slow scatter plot from simulation is shown in Fig. 5.

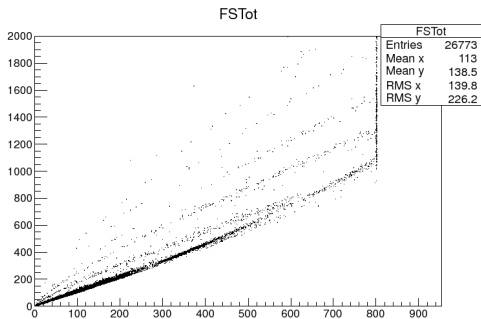


Figure 5: Fast vs Slow scatter plot simulated for Au+Au system.

The obtained fast-slow scatter plots have been treated in the same way as experimental data. Thus, the Grid KaliVeda library was used to identify the particles in charge and mass.

The same framework analysis, Fairroot, was used to perform the identification and preliminary analysis and some plots are shown in Fig. 6.

The comparison between Fig. 6a, presenting transverse velocity versus rapidity in lab reference system after detector filter, and Fig. 3a shows a similar behavior; in both cases projectile and target regions are clearly visible. A comparison of multiplicity distribution is shown in panel b).

In the legend, from tree (blue line) indicates the spectrum obtained after detector filter, while red line shows the simulated data filtered only for the geometrical acceptance of the detector, e.g. polar angle covered by CHIMERA ( $7^\circ$ - $20^\circ$ ); comparing the two distributions, we can investigate

the effect of detector in physics observables; in the same plot, green line shows total multiplicity from UrQMD simulation.

In panel c) we show the distribution of the total charge collected by CHIMERA as obtained after the detector replica, compared to the one obtained cutting only in polar angle; we can see that some fraction of the charge is lost when CHIMERA filter is used. The same comparison for the total charge collected in the ring N. 7, polar angle between 16 and 20 degrees, is presented in the panel d). A smaller distortion is then obtained.

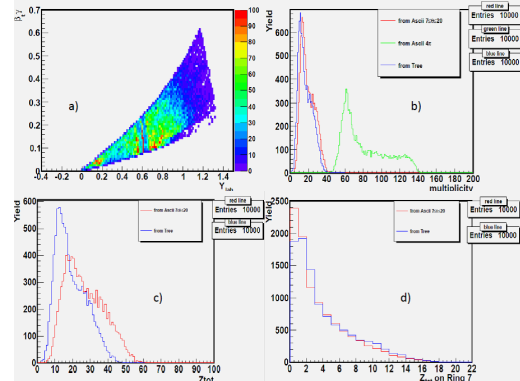


Figure 6: Data Simulation for Au+Au system; a) transverse velocity versus rapidity in lab reference system; b) multiplicity distribution; c) charge distribution; d) charge distribution only for polar angle covered by ring 7 of CHIMERA ( $16^\circ$ - $20^\circ$ ).

## References

- [1] Li Bao-An *et al.* *Phys. Rep.* **464**, 113 (2008).
- [2] Li Q *et al.* *Phys. Rev. C* **83**, 044617 (2011).
- [3] Russotto P *et al.* *Phys. Lett. B* **697**, 471 (2011).
- [4] Cozma M D *Phys. Lett. B* **700**, 139 (2011).
- [5] Giordano V. *et al.* *Phys. Rev. C* **81**, 044611 (2011).
- [6] Blaich Th *et al.* *Nucl. Instr. and Meth. A* **314**, 136 (1992).
- [7] Lukasik J *et al.* *Proceedings of IWM2011, EPJ Web of Conferences* **31**, 00032 (2012) and refs therein.
- [8] Schüttauf A *et al.* *Nucl. Phys. A* **607**, 457 (1996).
- [9] Sarantites D G *et al.* *Nucl. Instr. and Meth. A* **381**, 418 (1996).
- [10] Pagano A *et al.* *Nucl. Phys. A* **734**, 504 (2004).
- [11] <http://www-win.gsi.de/daq>.
- [12] Acosta L *et al.* *2011 IEEE Nucl. Sci. Symp. Conf. Rec.*, 202 (2011).
- [13] Andronic A *et al.* *Eur. Phys. J. A* **30**, 31 (2008).
- [14] Danielewicz P *et al.* *Phys. Lett. B* **157**, 146 (1985).
- [15] Ollitrault J-Y *arxiv:nucl-ex/971003*.